Colloids and Surfaces A: Physicochemical and Engineering Aspects 654 (2022) 130181

Contents lists available at ScienceDirect

Colloids and Surfaces A: Physicochemical and Engineering Aspects

journal homepage: www.elsevier.com/locate/colsurfa

Biomolecules adsorption to trigger the self-assembly of nanospheres and nanorods

Vikram Singh Raghuwanshi *, Maoqi Lin, Gil Garnier *

Bioresource Processing Research Institute of Australia (BioPRIA), Department of Chemical and Biological Engineering, Monash University, Clayton, Vic 3800, Australia

GRAPHICAL ABSTRACT

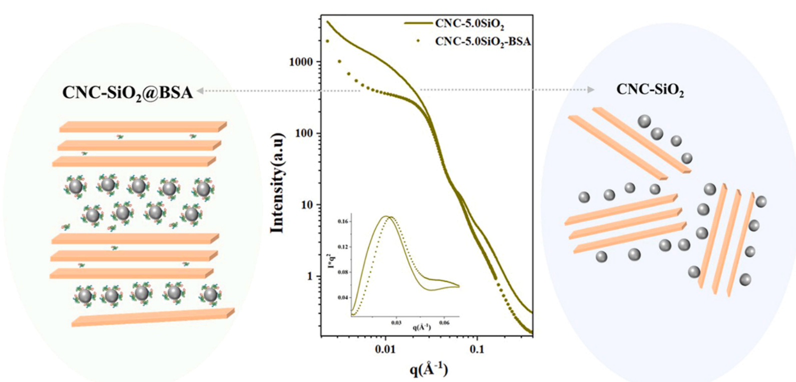

ARTICLE INFO

Keywords:
Self-assembly
Cellulose nanocrystals (CNC)
Nanorod
Silica (SiO_2)
Nanospheres
Biomolecules
Dynamic light scattering (DLS)
Small angle X-ray scattering (SAXS)
UV-Vis Spectroscopy (UV-Vis)
Quartz crystal microbalance with dissipation (QCM-D)
Bovine serum albumin (BSA)

ABSTRACT

Hypothesis: The self-assembly (SA) of nanostructures triggered by the adsorption of biomolecules (BSA) is investigated as a platform to develop diagnostics and functional applications. Mixing nanostructures of different morphologies; SiO_2 nanospheres (NS) to a cellulose nanorod crystals (CNC) leads to the formation of short range ordered domains in the dried film. Adding biomolecules-treated SiO_2 NS into the CNC develop the long range ordered assembly in the composite film.

Experiments: The CNC-SiO_2 composite films were prepared by mixing CNC suspension (3 wt%) with the SiO_2 NS of different concentration (0.5–5 mg/mL) followed by drying at the ambient conditions. The CNC-SiO_2 @BSA films are prepared by first mixing the BSA (1 mg/mL) with the SiO_2 suspension of different concentrations. Later the SiO_2 @BSA suspension was mixed with the CNC and left for drying at the ambient conditions. The self-assembly mechanisms of CNC, SiO_2 and BSA are studied by combining SEM, DLS, UV-Vis, QCM-D and SAXS analysis.

Findings: The SA mechanism of aqueous suspensions of CNC blended with SiO_2 NS pre-treated with BSA (by adsorption) is studied by a combination of small angle X-ray scattering (SAXS), scanning electron microscopy (SEM), UV-Vis spectroscopy (UV-Vis), dynamic light scattering (DLS) and quartz crystal microbalance with dissipation (QCM-D). Both CNC and SiO_2 NS are negatively charged and have demonstrated self-assembly ability driven from a combination of long- and short- range order arrangement. Adding SiO_2 NS to a CNC suspension

* Corresponding authors.
E-mail addresses: vikram.raghuwanshi@monash.edu (V.S. Raghuwanshi), gil.garnier@monash.edu (G. Garnier).

https://doi.org/10.1016/j.colsurfa.2022.130181
Received 20 July 2022; Received in revised form 10 September 2022; Accepted 12 September 2022
Available online 13 September 2022

disrupts the original SA of both CNC and SiO_2, which leads to the formation of small, short- range ordered domains of large polydispersity. Surprisingly, adding BSA-treated SiO_2 NS into the CNC network enhances the arrangement of CNC and NS towards a new system with long range ordered assembly. The SA mechanisms of cellulose-SiO_2 composites result from the balance of electrostatic repulsion and van der Waal attraction in the structure factor, radial distance distribution and potential of mean force. Understanding the effect of biomolecule adsorption on the self-assembling mechanisms of CNC nanorods with SiO_2 nanospheres enables the efficient engineering of catalysis, biosensors and diagnostics.

1. Introduction

The self-assembly (SA) of constituent nanomaterials (1–100 nm) can lead to composites with unique sets of mechanical, electronic, magnetic and optical properties [1–3]. Engineering such properties enables high performance functional composites for applications in imaging [4], catalysis [5], drug delivery [6], bioengineering [7,8], biosensors [9], and bio-diagnostics [9,10]. SA is the spontaneous arrangement of materials into a long- or short- range order driven by the balance of electrostatic, steric, ionic, hydrophobic, depletion and van der Waal interactions [11]. Different organic and inorganic materials in form of crystals, colloids, proteins and lipid layers have the intrinsic ability to self-assemble in an ordered or aggregated structure once in suspension [12]. Blending different nanomaterials with controlled SA can produce composites with novel properties and functionality.

Cellulose nanorod crystals (CNC) and silica (SiO_2) nanospheres are two materials of choice for their abundance, non-toxicity and renewability; they are biocompatible, have high surface areas, unique optical properties and are low cost [13]. CNC are rod shaped (D:5–20 nm, L: 100–200 nm) particles that self-assemble in a chiral nematic organisation to exhibit iridescence colours, both in suspension and their dried films [14]. Similarly, SiO_2 nanospheres are prone to self-assemble at the solid-liquid interface into composites showing opal like photonic crystals property [15]. However, it remains challenging to optimise the self-assemble photonic structures of CNC and SiO_2 to work effectively in broad range of applications [16–18].

Mixing negatively charged SiO_2 nanospheres with anionic CNC forms transparent composite films. Optimising the SA of CNC nanorods and SiO_2 nanospheres produces composites of novel properties for innovative applications [19]. Recently, we have shown that incorporation of CNC nanorods in graphene oxide (GO) sheet suspension aligns the GO sheets in the direction of the CNC nematic arrangement [20]. SA of different nanostructures in a composite depends on their morphology, size, concentration and surface properties [21]. It is difficult to control SA of nanostructures incorporated in a composite in a desired structure. Still many questions and challenges remain to understand the SA mechanisms of nanostructures in composites. It is unclear which dominating interacting forces bring the nanostructures together at the equilibrium distance and in a specific order. Furthermore, how the surface properties, different morphologies and concentration of nanostructures influence the SA in a composite remains obscure. There is a need for a better fundamental understanding of the SA mechanisms of individual components and their mixture in a composite.

In this study, we control the self-assembly of SiO_2 nanospheres and CNC nanorods by adsorbing BSA onto the SiO_2. Free standing composite films of CNC, CNC-SiO_2 and CNC-SiO_2 with adsorbed BSA (SiO_2 @BSA) were produced by evaporation of water under ambient conditions. The SA mechanism is quantified by combining high flux synchrotron small angle X-ray scattering (SAXS) with scanning electron microscopy (SEM), dynamic light scattering (DLS), UV-Vis spectroscopy (UV-Vis), and quartz crystal microbalance (QCM) measurements. We evaluate the effect of interparticle distance, CNC pitch size, biomolecules conformation, and interparticle interaction by structure factor, radial distance distribution and potential mean force. The knowledge gained on the nanoscale SA mechanisms of nanostructures can help to create versatile and inexpensive functional composites for advanced optical and biomedical applications.

2. Experiments

2.1. Materials

The cellulose nanocrystals (CNC) were purchased from the University of Maine, USA. The initial concentration of the CNC is 10 wt% which is diluted to 3 wt% in the MilliQ water. The SiO_2 nanoparticles (PL-1) were purchased from the company FUSO chemical Co. Ltd., Japan. The initial SiO_2 nanoparticle concentration was 12 wt% and primary particle size of 15 nm and secondary particle of 40 nm with the aggregation ratio of 2.7. The SiO_2 suspension was diluted to different concentration from 0.5 mg/mL to 5 mg/mL in the MilliQ water. The Bovine serum albumin (BSA) protein is purchased from Sigma Aldrich (Merk) with the molecular weight of 66,000 Da and size of 4 nm x 4 nm x 12 nm. The BSA was in the powder form and used as without any further purification. The BSA was diluted to the 1 mg/mL in the MilliQ water.

2.2. CNC-SiO_2 composites

The CNC-SiO_2 films were prepared by adding CNC suspension (3 wt %) with the SiO_2 with different concentration in the glass vials and mixed in a vortex for a 1 min at 1400 rpm. The CNC-SiO_2 suspension is poured in the plastic container of volume 5 mL. The suspension is left for drying in the open air at the ambient condition. The suspension is dried in 48 h. The dried film is peeled off from the container and used for the measurement. All films are optically transparent. The CNC-SiO_2 @BSA is prepared by first mixing the BSA (1 mg/mL) with the SiO_2 suspension of different concentrations. Later the SiO_2 @BSA suspension was mixed with the CNC and vortex for 1 min. The CNC-SiO_2 @BSA suspension is poured into the container and left for drying at the ambient conditions.

2.3. Scanning electron microscopy (SEM)

The SEM measurements were made on the cross-section of the CNC-SiO_2 and CNC-SiO_2 @BSA free standing films. For the SEM a FEI Magellan 400 FEGSEM instrument was used. The samples were coated with iridium (<1 nm) to avoid charging effects during SEM measurements.

2.4. Small angle X-ray scattering (SAXS)

SAXS measurements were performed at the Australian synchrotron with high photon flux to generate strong statistics for the data analysis [22]. All samples were measured in the transmission mode by using the X-ray energy of 12 KeV. A Pilatus detector with the pixel size of 70 μm x 70 μm was used to collect the scattered X-rays. The exposure time is between 1 and 5 s. The liquid samples were filled in the quartz capillary of thickness 1 mm. Different standards of glassy carbon and silver behenate is used to calibrate the scattering curves to the absolute units and the q values. Background scattering from air is subtracted from the scattering data of the composite films. Scattering from water filled capillary is used as background for the liquid samples. The data reduction and averaging of the scattering images were performed using the inhouse software Scatterbrain [33].

2.5. Dynamic light scattering (DLS)

The dynamic light scattering experiments were performed on the Brookhaven NanoBrook instrument equipped with the red laser of wavelength 600 nm. The plastic cuvettes of 3 mL in volume were used. Both zeta potential and hydrodynamic size was measured. Different set of experiments were made and averaged to get the final value of the zeta potential and particle size. First, the pure silica nanospheres were measured and later the SiO_2 adsorbed with the BSA was measured at the room temperature.

2.6. UV−Vis spectroscopy (UV-Vis)

UV−Vis measurements were performed on the UV–Vis spectrometer

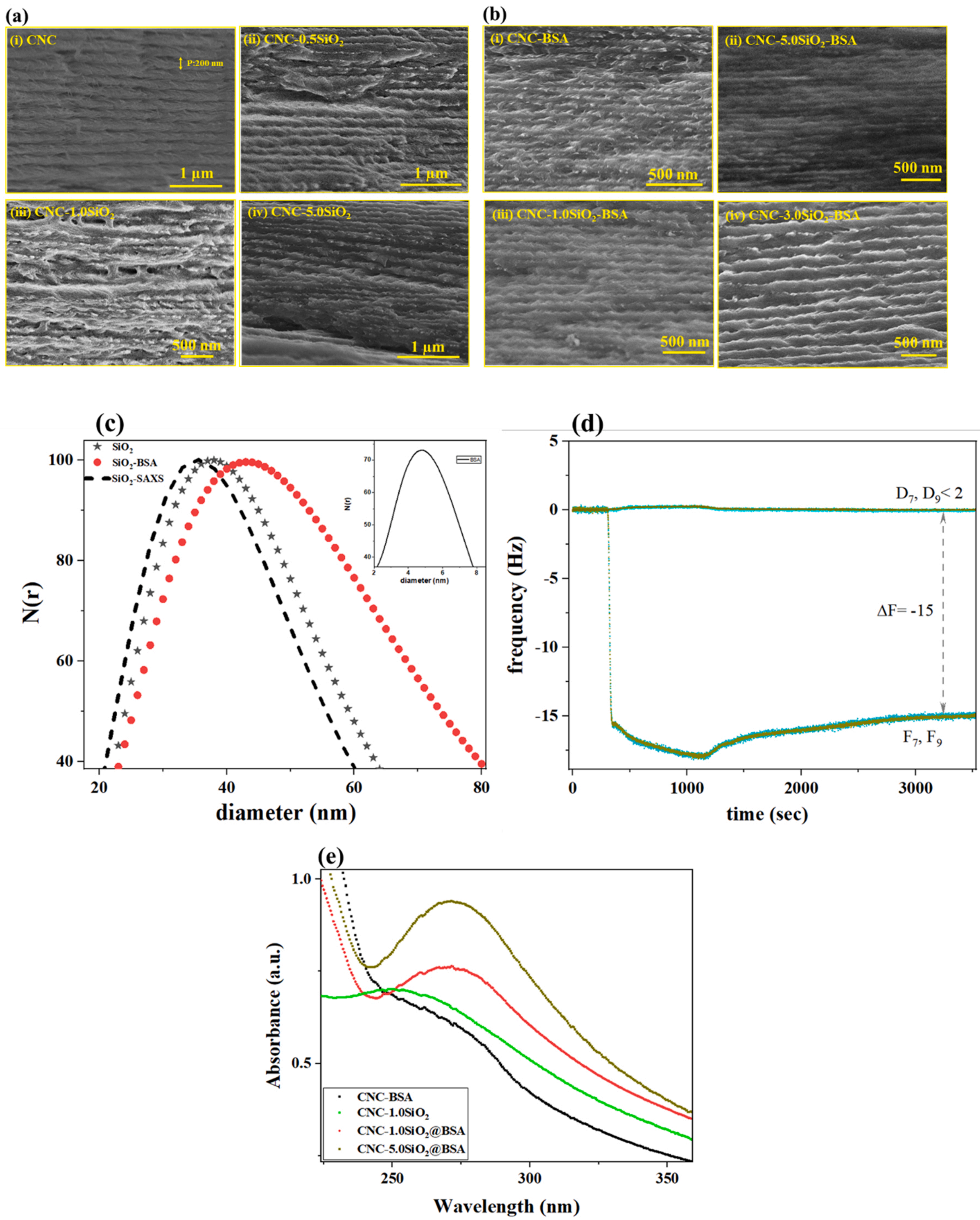

Fig. 1. (a). SEM micrograph of (i) pure CNC and CNC containing different amount of SiO_2 NS: (ii) 0.5 mg/mL, (iii) 1 mg/mL, (iv) 5 mg/mL. (b). (i) SEM micrograph of CNC blended with BSA and CNC blended with different amounts of SiO_2 NS pre-adsorbed with BSA at 1 mg/mL; The SiO_2 concentration varies as: (ii) 0.5 mg/mL, (iii) 1 mg/mL, (iv) 3 mg/mL. (c). Size distribution obtained by Dynamic Light Scattering (DLS) for the pure SiO_2, and SiO_2 treated with 1 mg/mL of BSA. Inset shows the DLS of pure BSA. The dashed lines show the size distribution extracted from the SAXS curve of 0.1 mg/mL SiO_2 aqueous suspension (d) QCM-D spectrogram for BSA adsorbed onto silica coated quartz crystals. (e) UV-Vis spectra for the CNC-BSA, CNC-1 mg/mL SiO_2, CNC-1 mg/mL SiO_2 pre-adsorbed with BSA and CNC-5 mg/mL SiO_2 pre-adsorbed with BSA.

(Cary 60 UV–vis Agilent Technologies) equipped with the Xenon flash lamp (80 Hz) light source. The samples were placed on the sample holder and the spectra were recorded between 200 and 700 nm at room temperature.

2.7. Quartz crystal microbalance with dissipation (QCM-D)

QCM-D measurements were made at the Q-sense E4 instrument using the Silica coated quartz crystal . In the measurement, first a stable base line was made by passing the MilliQ water through the module. Later, the BSA solution of concentration 1 mg/mL at pH-8 pass through the module at the flow rate of 150 μL/min. The adsorption of BSA was measured kinetically for 20 min and rinsed with the MilliQ water to remove all the non-adsorbed BSA. Different frequency F_3, F_5, F_7 with the dissipation D_n were recorded with variation in the adsorption time. The Q-tools software was used to extract the raw data.

3. Results

The composite films of CNC, CNC-SiO_2 and CNC-SiO_2 @BSA are prepared by drying an aqueous suspension of 3 wt% CNC blended with different concentrations of SiO_2 nanospheres (NS) and SiO_2 @BSA. At first glance, all films are optically transparent, indicating that the self-assembled nanostructures domain size in the composites are smaller than the visible wavelength of light (< 400 nm). The visible light passes through the films without any reflection or scattering so the films appear transparent. Next, the nanostructures SA mechanisms in the composites are determined by measuring the CNC pitch size, interparticle distance and strength of interparticle interactions.

Scanning electron microscopy (SEM) reveals the structural arrangement of pure CNC, and CNC-SiO_2 at concentrations ranging from 0.5 mg/mL to 5 mg/mL (Fig. 1a). For pure CNC, the horizontal lines are homogeneously arranged with specific inter-line spacing indicating a chiral nematic arrangement of the CNC rods. The half-pitch size of 200 nm is measuring the distance between two consecutive lines (Fig. 1a.i). Adding SiO_2 NS disrupts this CNC self-assembly which is noticed by the dissimilarity in the horizontal line arrangement (Fig. 1a. (ii-iv)). Disturbance in the CNC rod arrangement reflects the different half-pitch sizes ranging between 50 and 200 nm. This indicates that the strong repulsion between the negatively charged CNC and SiO_2 inhibits their SA in the composite.

The effect of pre-adsorbing BSA onto SiO_2 NS in the CNC composites was then investigated. The DLS measurements confirm the adsorption of BSA onto SiO_2. In Fig. 1c without BSA, SiO_2 has a mean size distribution of 38 nm, which increases to 44 nm upon BSA adsorption. The BSA adsorption layer onto the SiO_2 NS is estimated to be 4–6 nm thick. The SAXS data analysis on the 0.1 mg/mL of SiO_2 aqueous suspension and BSA 1 mg/mL aqueous suspension achieved by fitting the experimental data with the sphere model reveals the particle size distribution to be comparable to the DLS measurements (Fig. 1c dashed lines). The scattering curves are provided in the supporting information (SI. 4). QCM-D measurements validate the DLS results and reveals BSA to adsorb at a surface coverage of 2.7 mg/m^2 onto silica coated quartz crystals (Fig. 1d). Details of the QCM-D analysis are provided in supporting information (SI.1). Previously, similar results were reported for BSA adsorption onto the negatively charged gold interface [23].

SEM micrographs of the composites made from CNC-BSA, CNC-SiO_2 @BSA (at different SiO_2 concentrations) are shown in Fig. 1b. The SEM for CNC-BSA shows organised CNC self-assembly with a smaller half-pitch size of 100 nm and some area of 200 nm (Fig. 1b (i)). Interestingly, the CNC-SiO_2 @BSA composites retain the original self-assembled structure of CNC but with a smaller pitch size. Furthermore, increasing the SiO_2 @BSA concentration in the composites increases the ordering of the CNC rods assembly without any significant variation in the pitch size. However, only by SEM, it is difficult to extract the complete SA characterisation of the composites. SEM is a direct real space imaging method which provides only local area information over a few micrometres' depth. Moreover, the SEM sample preparation can create misleading artefacts. Thus, a complementary perspective of the self-assembly of CNC, SiO_2 and SiO_2 @BSA in the composites film over a complete volume was performed by UV-Vis spectrometry and SAXS analysis. UV-Vis provides qualitative information on the ordering of the nanostructures [37]. SAXS is a powerful analytical method which determines the nanoscale assembly over complete volume at scales ranging from 1 to 100 nm [24–26].

Fig. 1e shows the UV-Vis spectra for the composite films of CNC treated with BSA (CNC-BSA), CNC with 1 mg/mL SiO_2 NPs (CNC-1.0SiO_2) and CNC with 1 and 5 mg/mL SiO_2 NPs pre-adsorbed with BSA. Both CNC-BSA and CNC-1.0SiO_2 show broad absorption peak spectra between 250 and 300 nm. Interestingly, CNC with pre-adsorbed BSA on the SiO_2 shows a sharp absorption peak which indicates an increase in the ordering of the NPs in the film. Further increase in the SiO_2 concentration (CNC-5.0SiO_2 @BSA) enhances the absorption peak sharpness (narrow full width at half-maxima:FWHM) revealing the presence of long-range assemblies of nanostructures in the film [38].

SAXS measurements are performed to determine the structural arrangement and self-assembly of CNC, CNC-SiO_2, CNC-BSA and CNC-SiO_2 @BSA nanostructures in the composite films. Fig. 2a.(i) compares the SAXS curve of the CNC and CNC-BSA films. The CNC film shows two correlation peaks with the primary peak centred at $q^* = 0.015$ Å^{-1} which reveals an inter-rod distance of 42 ± 1 nm. The interparticle distance 'd' is determined by the relation: $d = 2\pi/q^*$. By adding BSA to CNC, the SAXS correlation peak shifts towards the high q value (q^*=0.021 Å^{-1}), which indicates a decrease in the interrod distance to 30 nm. This is consistent with the SEM analysis which shows the original half-pitch size of CNC films of 200 nm reduced nearly by half (100 nm) for the CNC-BSA films. This indicates that BSA adsorbs onto CNC which reduces the inter rod repulsion, bringing the CNC rods closer to each other. However, adding BSA does not disrupt the order of the CNC rods in the chiral nematic structures.

Fig. 2a(ii) shows the SAXS curves of the CNC-SiO_2 composite films with increasing concentrations of SiO_2. At lower SiO_2 content, the SAXS curve peak becomes broader, indicating the disruption of the CNC self-assembly. The correlation peak at q^* =0.0228 Å^{-1} gives an interparticle distance of 27.5 ± 0.4 nm. Upon further increasing the SiO_2 concentration, the SAXS curve intensity increases and the peak at the lower q values becomes broader. The clarity of the peak is better seen in the Kratky plot (SI. 2). The primary correlation peak in the Kratky plot fits well with the Gaussian shape function. The correlation peak shifts towards higher q values at q^* =0.0238 Å^{-1}, revealing a decrease in interparticle distance to 26.4 ± 0.3 nm, which remains constant for higher SiO_2 concentrations (≥ 1 mg/mL). The Gaussian fit Kratky plots for the CNC-0.5SiO_2 and CNC-5.0SiO_2 are provided in the supporting information (SI. 2). The increase in the SAXS intensity with SiO_2 concentration simply follows the higher SiO_2 volume fraction in the film. The power law slope q^{-3} at the higher q values reveals scattering from the surface of nanostructures. However, the upturn in the scattering intensity at the end of the lower q value indicates the presence of larger structures formed by different arrangement of nanostructures.

Fig. 2a.(iii) shows the SAXS curves of the CNC-SiO_2 @BSA films. The broadness of the SAXS peak decreases compared to CNC-SiO_2. The Kratky plot is shown in supporting information (SI. 2). Fig. 2b (i-iv) compares the SAXS curve profile of CNC-SiO_2 composites with the CNC-SiO_2 @BSA at different SiO_2 concentrations. The inset shows the Kratky plot comparison of the respective SAXS curves. The correlation peak for 0.5 mg/mL SiO_2 @BSA is observed at q^* =0.0245 Å^{-1} which corresponds to an interparticle distance of 25.6 ± 0.4 nm. As increases the SiO_2 @BSA concentration, the correlation peak shifts toward a higher q value of q^* =0.027 Å^{-1} for 5 mg/mL SiO_2 @BSA. This indicates a decrease in the interparticle distance from 25.6 nm to 23.6 ± 0.3 nm. Without BSA, the interparticle distance remains constant at 26.4 nm (Fig. 2 c.i). The CNC-SiO_2 @BSA composite has a sharper peak (small

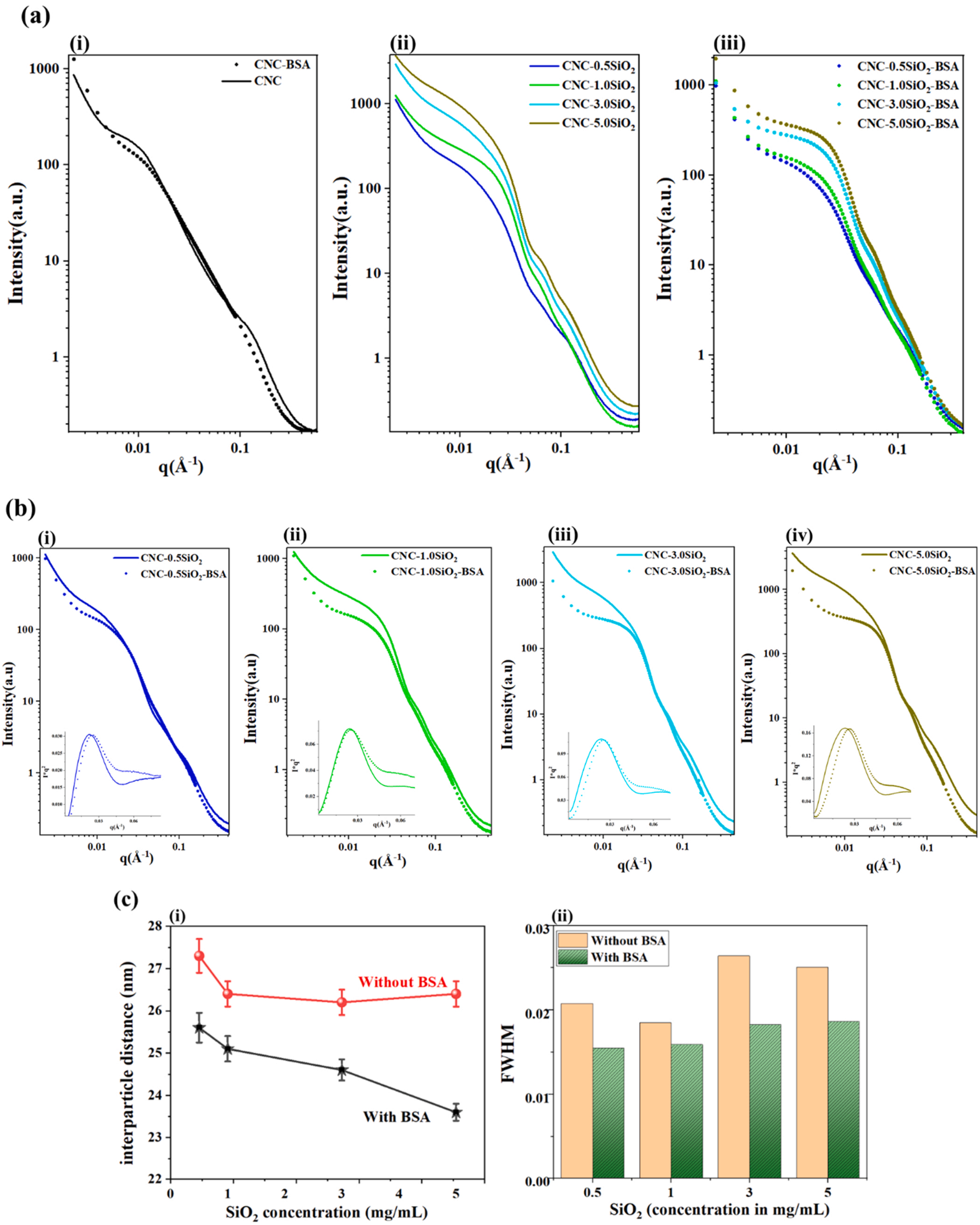

Fig. 2. (a). SAXS curves of: (i) pure CNC and CNC blended with BSA, (ii) CNC with different concentrations of SiO_2 (0.5 – 5 mg/mL), (iii) CNC with different concentrations of SiO_2(0.5 – 5 mg/mL) treated with BSA (1 mg/mL) (b). Comparison of SAXS curves of CNC with different concentrations of SiO_2 and SiO_2 @BSA: (i) 0.5 mg/mL (ii) 1 mg/mL, (iii) 3 mg/mL, (iv) 5 mg/mL. Inset shows the Kratky plot of the SAXS curves (c): (i) Plot of interparticle distance as a function of SiO_2 concentration, (ii) Full width at half maxima (FWHM) of the peak close to q= 0.023–0.027 $Å^{-1}$ as a function of SiO_2 concentration.

full width at half maxima: FWHM) than the CNC-SiO_2 composites (Fig. 2 c.ii). This indicates that BSA increases the correlation length of the ordered structure, as observed by SEM.

Further information from SAXS curves is extracted by fitting them with the shape model of a sphere and a long cylinder for the CNC-SiO_2 composites. For the CNC-SiO_2 @BSA, a spherical core-shell shape model combined with the long cylinder shape is selected. For the interparticle interaction, a structure factor (SF) is introduced which reveals the interparticle interaction between the nanostructures in the composites. More information on SAXS curves fitting procedure and fitted SAXS curves are provided in supporting information (SI. 3 & 4). The SF is extracted from the SAXS curve fitting for all samples, with and without BSA (Fig. 3a). The CNC-SiO_2 composite has a broad SF peak which shows weak interparticle interactions. As increases the SiO_2 concentration, the peak narrows; however, the interparticle interactions remain weak. This is expected due to the high negative charge on both SiO_2 and CNC stabilising by electrostatic repulsion, hindering assembly. Interestingly, the SF peak for CNC-SiO_2 @BSA is sharper and of higher intensity than for CNC-SiO_2. As increases the SiO_2 @BSA concentration, the SF peak intensity and sharpness both increase indicating stronger interparticle interaction.

The radial distribution function (RDF) evaluated from the SF shows the surrounding nanoparticles distribution (Fig. 3b). The RDF is determined by the relation:

$$G(r) = 1 + \frac{1}{2\pi^2 r}\int_{q_{min}}^{q_{max}} q.(S(q) - 1).\sin(q.r)dq \quad (1)$$

Where, S(q) is the structure factor, q_{max} and q_{min} are the maximum and minimum q values in the scattering curves, respectively. The RDF for CNC-SiO_2 @BSA has multiple peaks (1st peak close to 250 Å, 2nd peak close to 400 Å and 3rd peak close to 500 Å) which reveals structural order in the arrangement of the nanostructures in the nearest neighbouring shells. As increases the SiO_2 @BSA concentration, the RDF peak becomes stronger and the second order peak is clearly visible. More SiO_2 @BSA particles are organised in a long-range order.

A potential of mean force φ(r) between the nanostructures is calculated from the RDF from the relation:

$$\varphi(r)/K_B T = \ln(1/G(r)) \quad (2)$$

Where, K_B is the Boltzmann constant and T is the absolute temperature. The $\varphi(r)$ for CNC-SiO_2 and CNC-SiO_2 @BSA composites is shown in Fig. 3c. CNC-SiO_2 composites display electrostatic repulsion between SiO_2 and CNC at all SiO_2 concentrations, revealed by the poor attractive potential of φ(r). For CNC-SiO_2 @BSA at lower SiO_2 concentration (0.5 mg/mL), there is an increase in the attractive force potential up to a distance of 26 nm, followed by repulsion at lower distances. The dip shows an equilibrium interparticle distance balanced from the attractive and repulsive forces. An increase in SiO_2 concentration (5 mg/mL) increases the dip value of attractive potential which shifts towards shorter interparticle distance from 26 nm to 24 nm. The higher attraction potential with increases in SiO_2 @BSA is due to BSA adsorption which screens the SiO_2 surface charge, reducing interparticle repulsion.

4. Discussion

Cellulose nanorod crystals (CNC) have the intrinsic property of self-

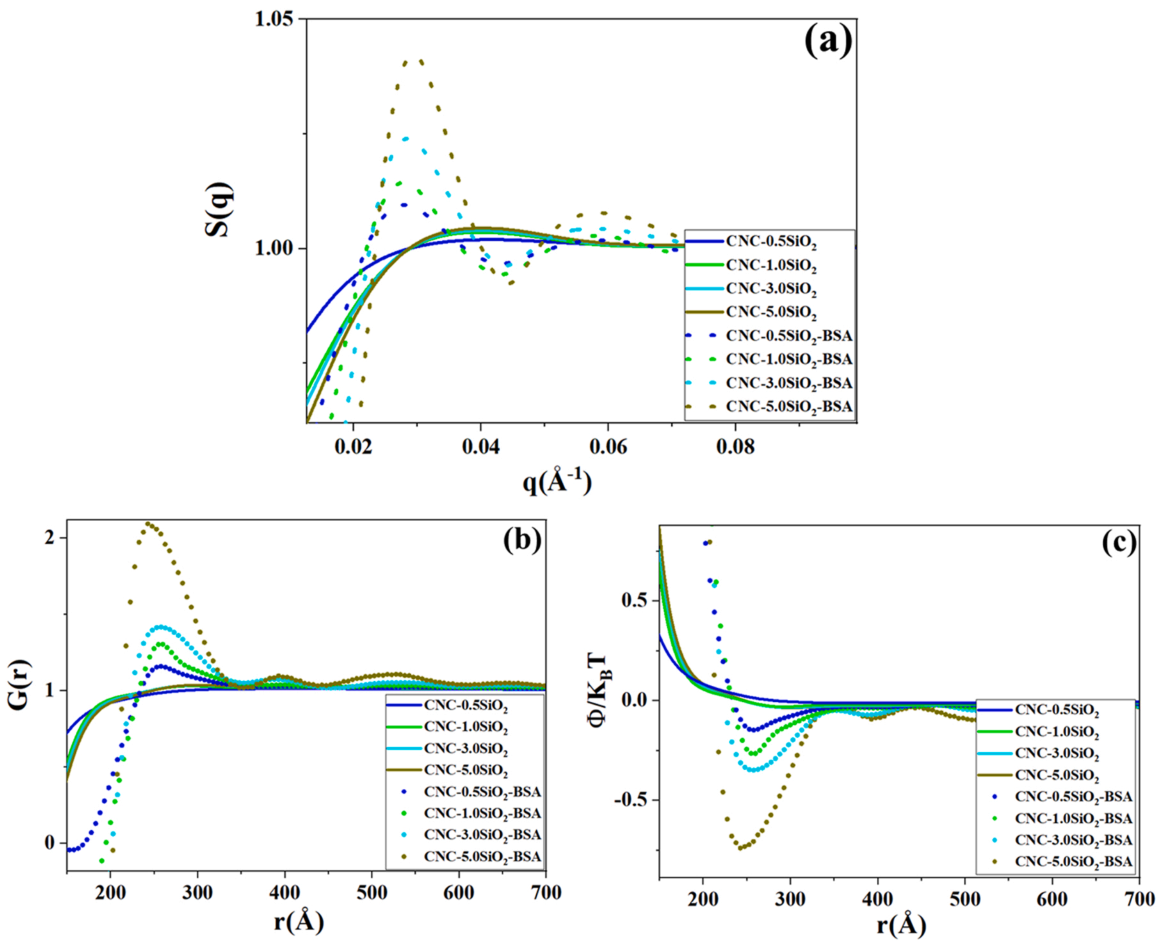

Fig. 3. (a) Structure factor extracted from SAXS curves fitting of CNC-SiO_2 and CNC-SiO_2 @BSA; (b) Radial distance distribution evaluated from the structure factor; (c) Potential mean force calculated from the radial distance distribution.

assembling into a chiral nematic structure [27,28]. Similarly, SiO_2 NS self-assemble in a long- and short- range order at different interfaces [29, 30]. Pure CNC in the dried film shows the chiral nematic arrangement with an interrod distance of 42 nm. Adding SiO_2 NS to the CNC network disrupts the original SA of both CNC and SiO_2 NPs (Figs. 1, 2, SEM and SAXS). The high negative zeta potential of CNC (−50 mV) and SiO_2 (−40 mV) repulses CNC from SiO_2 NS. In the dried CNC-SiO_2 composites at lower SiO_2 concentration (0.5 mg/mL), the CNC are far apart with an interparticle distance of 27.5 ± 0.4 nm; interparticle interaction is weak as revealed by broad peak in structure factor analysis (Fig. 3a). Both SiO_2 and CNC attempt to self-assemble in an ordered structure. However, during drying, the electrostatic repulsions lead to the formation of smaller domains of CNC, SiO_2 and mixed CNC-SiO_2 (Fig. 4. Left).

An increase in the SiO_2 NS concentration leads to an increase in the domain size of the SiO_2 NS which inhibits the long-range SA of CNC. The interparticle distance of CNC in the domains decreases from 27.5 ± 0.4 nm to 26.4 ± 0.3 nm and does not vary with further increase in SiO_2 concentration up to 5 mg/mL. These CNC domains are separated by the intercalation of short-range SiO_2 NS domains. However, within these domains, the interparticle interaction is weak and does not change upon an increase in the SiO_2 NPs concentration; this is demonstrated by the broad structure factor analysis. The SEM micrographs validate the SAXS results as adding SiO_2 NS disrupts this CNC self-assembly as observed in the dissimilarity in the horizontal line arrangement.

Initially, both CNC and SiO_2 have electrostatic repulsions once in suspension which repel them from each other. As the water molecules evaporate, the CNC rods come closer and assemble by forming a network of hydrogen bonding. SiO_2 NS also form domains intercalated between those of CNC. Since both CNC and SiO_2 are negatively charged, the force balance between electrostatic repulsion, van der Waal and hydrogen bonding leads to the formation of a free-standing film.

BSA adsorbs onto SiO_2 NS and significantly affects the assembling of CNC and SiO_2 @BSA in the composites. Adsorbing BSA onto SiO_2 induces self-assembling arrangement in a long-range order compared to the original CNC-SiO_2 composites without BSA. Adding BSA increases the order of the SiO_2 domains formed. The enhancement in the UV-Vis absorption peak sharpness (narrow FWHM) supports the long-range self-assembly of nanostructures in the film. BSA is highly negatively charged at pH 8; however, it adsorbs over the negatively charged SiO_2 as recorded by QCM and DLS (Figs. 1c and 1d). The negatively charged BSA adsorb both onto the negatively charged SiO_2 and the gold interface by different interactions as previously reported [23,31].

The SAXS curves show sharper correlation peaks (lower FWHM) as increases the SiO_2 @BSA NPs concentration, revealing an increase in the long-range order (Fig. 2 c.ii). BSA adsorbs and neutralises the charge of the SiO_2 nanospheres which decreases the interparticle repulsive force, reducing the inter CNC rod distance to 25.6 ± 0.4 nm. There is also some free BSA in the suspension which adsorbs onto the CNC, contributing in decreasing the inter-rod distance which reduces the pitch size as observed in the SEM micrographs (Fig. 1b). A decrease in the interparticle distance also increases the interparticle interaction as seen by the sharpness of the structure factor peak (Fig. 3a). SEM images confirm an increase in the ordering of the CNC rods assembly in the presence of BSA compared to the CNC-SiO_2 composite without BSA. Further addition of SiO_2 @BSA at higher concentration leads to a further decrease in the inter CNC rod distance to 23.6 ± 0.3 nm. Thus, adding BSA controls the self-assembly of both CNC and SiO_2. BSA reduces the strong electrostatic repulsion between CNC and SiO_2, enabling self-assembling in the ordered long- and short-range individual domains (Fig. 4. Right). Capillary forces play an important part in the self-assembly of nanostructures. There are different capillary forces acting between the colloidal particles of variable shape and size; (i) SiO_2 NS- SiO_2 NS, (ii) SiO_2 NS- CNC rods, and (iii) CNC rod -CNC rod. This leads to different liquid meniscus between different interfaces during flotation and immersion of particles (with and without BSA) in the system [34]. Despite advancement in this field, complex mathematics and systematic study are required to deal with the capillary force driving directional self-assembly of different shape nanostructures in the composite film [35,36]. Thus, in this study we have restricted ourselves to apply simple methodologies for the explanation of the self-assembly mechanism of CNC nanorods and SiO_2 nanospheres in composite films. It would be interesting for future study to reveal the effect of neutral/low charge polymer or weakly charged nanoparticle on the SA of nanostructures of different morphologies.

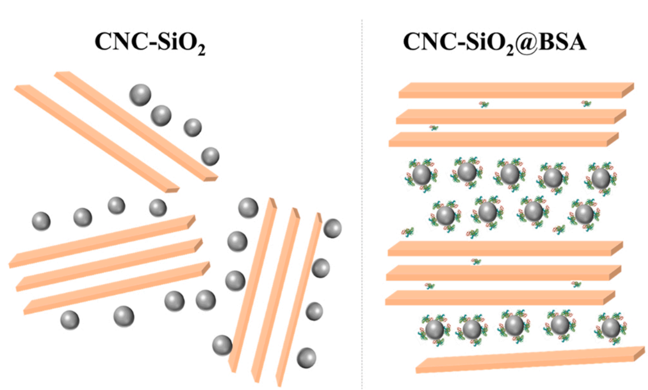

Fig. 4. (Left) Schematic of the CNC and SiO_2 arrangement in the CNC-SiO_2 composites. (Right) Schematic of the effect of BSA treated SiO_2 on the CNC and SiO_2 @BSA arrangement in the CNC-SiO_2 @BSA composites.

5. Conclusion

This study analyses the effect of protein adsorption (BSA) onto Silica (SiO_2) has on the structure of Cellulose NanoCrystals (CNC)- SiO_2 suspensions and their dried films. The evaporation induced spatial self-assembly (SA) of CNC, SiO_2 and SiO_2 @BSA are revealed in CNC-SiO_2 and CNC-SiO_2 @BSA dried composite films by combining SAXS, SEM, UV-Vis, DLS and QCM-D measurements. In a CNC-SiO_2 film, lower SiO_2 concentrations disrupt the original SA of both CNC and SiO_2 NPs. The CNC and SiO_2 components self-assemble individually into short-range ordered domains driven by the weak interparticle interactions. These domains are randomly distributed in the film. Increasing the SiO_2 concentration increases only the size of the SiO_2 domains with slightly smaller interparticle distance and weaker interparticle interaction, as revealed by a broad peak in structure factor. The CNC domains are smaller and positioned as separators between the SiO_2 domains. Interestingly, composites of SiO_2 pre-adsorbed with BSA (SiO_2 @BSA) and CNC show an increase in the ordering of the SA SiO_2 @BSA and CNC domains linked with stronger interparticle interaction. BSA reduces the SiO_2 surface potential which decreases electrostatic repulsions and increases the interparticle interaction. The strong interaction substantially decreases the interparticle distance between SiO_2 @BSA from 27 nm to 23 nm. The lower surface potential of SiO_2 @BSA also reduces the electrostatic repulsions between CNC and SiO_2 @BSA, which brings the CNC rods closer to the SiO_2 @BSA domains. This reduction in electrostatic repulsion balanced by van der Waal attraction leads to controlled and well-ordered self-assemblies of CNC and SiO_2 @BSA in the composites. Previously, nanostructures of different morphologies led to the formation of composites films exhibiting randomly distributed short-ranged SA domains of nanostructure [19,32]. This study demonstrates that the self-assembling of SiO_2 nanospheres and CNC nanorods can be controlled and modulated by varying the surface properties through biomolecules adsorption. The gained fundamental knowledge enables to engineer biodegradable composites exploiting the functionality of CNC, SiO_2 and biomolecules for generating structural colours, sensor, and bio diagnostic applications.

CRediT authorship contribution statement

Vikram Singh Raghuwanshi: Supervision, Investigation, Data curation, Methodology, Writing – original draft, Writing – review & editing. **Maoqi Lin**: Data curation. **Gil Garnier**: Supervision, Writing – review & editing.

Declaration of Competing Interest

The authors declare that they have no known competing financial interests or personal relationships that could have appeared to influence the work reported in this paper.

Data availability

Data will be made available on request.

Acknowledgements

The authors would like to acknowledgment the Australian Research Council (ARC) - Industrial Transformation Hub Grant HI130100016. The authors thank to Nigel Kirby, Stephen Mude and the SAXS/WAXS beamline at the Australian Synchrotron for the SAXS measurements and Australian nuclear science and technology organisation (ANSTO) for the beamtime.

Appendix A. Supporting information

Supplementary data associated with this article can be found in the online version at doi:10.1016/j.colsurfa.2022.130181.

References

[1] K. Stratford, O. Henrich, J.S. Lintuvuori, M.E. Cates, D. Marenduzzo, Self-assembly of colloid-cholesteric composites provides a possible route to switchable optical materials, Nat. Commun. 5 (1) (2014) 3954.
[2] M.H. Bistervels, M. Kamp, H. Schoenmaker, A.M. Brouwer, W.L. Noorduin, Light-controlled nucleation and shaping of self-assembling nanocomposites, Adv. Mater. 34 (5) (2022), 2107843.
[3] G.M. Whitesides, B. Grzybowski, Self-assembly at all scales, Science 295 (5564) (2002) 2418–2421.
[4] P. Martinez Pancorbo, K. Thummavichai, L. Clark, T.A. Tabish, J. Mansfield, B. Gardner, H. Chang, N. Stone, Y. Zhu, Novel Au–SiO2–WO3 core–shell composite nanoparticles for surface-enhanced Raman spectroscopy with potential application in cancer cell imaging, Adv. Funct. Mater. 29 (46) (2019), 1903549.
[5] S. Liu, P. Du, H. Sun, H.Y. Yu, Z.G. Wang, Bioinspired supramolecular catalysts from designed self-assembly of DNA or peptides, ACS Catal. 10 (24) (2020) 14937–14958.
[6] J. Yang, H.W. An, H. Wang, Self-assembled peptide drug delivery systems, ACS Appl. Bio Mater. 4 (1) (2021) 24–46.
[7] B.H.A. Rehm, Bioengineering towards self-assembly of particulate vaccines, Curr. Opin. Biotechnol. 48 (2017) 42–53.
[8] T. Shimizu, H. Minamikawa, M. Kogiso, M. Aoyagi, N. Kameta, W. Ding, M. Masuda, Self-organized nanotube materials and their application in bioengineering, Polym. J. 46 (12) (2014) 831–858.
[9] S. Huang, Y. Song, Z. He, J.R. Zhang, J.J. Zhu, Self-assembled nanomaterials for biosensing and therapeutics: recent advances and challenges, Analyst 146 (9) (2021) 2807–2817.
[10] N.L. Rosi, C.A. Mirkin, Nanostructures in biodiagnostics, Chem. Rev. 105 (4) (2005) 1547–1562.
[11] D.V. Talapin, M. Engel, P.V. Braun, Functional materials and devices by self-assembly, MRS Bull. 45 (10) (2020) 799–806.
[12] S. Förster, T. Plantenberg, From self-organizing polymers to nanohybrid and biomaterials, Angew. Chem. Int. Ed. 41 (5) (2002) 688–714.
[13] Y. Habibi, L.A. Lucia, O.J. Rojas, Cellulose nanocrystals: chemistry, self-assembly, and applications, Chem. Rev. 110 (6) (2010) 3479–3500.
[14] J. Shojaeiarani, D.S. Bajwa, S. Chanda, Cellulose nanocrystal based composites: a review, Compos. Part C Open Access 5 (2021), 100164.
[15] J.V. Sanders, Colour of precious opal, Nature 204 (4964) (1964) 1151–1153.
[16] V. Selvarajan, S. Obuobi, P.L.R. Ee, Silica nanoparticles—a versatile tool for the treatment of bacterial infections, Front. Chem. 8 (2020) 602.
[17] M. El-Shetehy, A. Moradi, M. Maceroni, D. Reinhardt, A. Petri-Fink, B. Rothen-Rutishauser, F. Mauch, F. Schwab, Silica nanoparticles enhance disease resistance in Arabidopsis plants, Nat. Nanotechnol. 16 (3) (2021) 344–353.
[18] Y. Li, N. Li, W. Pan, Z. Yu, L. Yang, B. Tang, Hollow mesoporous silica nanoparticles with tunable structures for controlled drug delivery, Acs Appl. Mater. Interfaces 9 (3) (2017) 2123–2129.
[19] K.E. Shopsowitz, J.A. Kelly, W.Y. Hamad, M.J. MacLachlan, Biopolymer templated glass with a twist: controlling the chirality, porosity, and photonic properties of silica with cellulose nanocrystals, Adv. Funct. Mater. 24 (3) (2014) 327–338.
[20] V.S. Raghuwanshi, S. Varanasi, W. Batchelor, G. Garnier, Cellulose nanocrystals to modulate the self-assembly of graphene oxide in suspension, Mater. Des. 216 (2022), 110572.
[21] S. Mohammed, H. Asgar, I. Kuzmenko, G. Gadikota, Self-assembly of silica nanoparticles at water-hydrocarbon interfaces: insights from in operando small-angle X-ray scattering measurements and molecular dynamics simulations, Energy Fuel 34 (10) (2020) 12545–12555.
[22] N.M. Kirby, S.T. Mudie, A.M. Hawley, D.J. Cookson, H.D.T. Mertens, N. Cowieson, V. Samardzic-Boban, A low-background-intensity focusing small-angle X-ray scattering undulator beamline, J. Appl. Crystallogr. 46 (2013) 1670–1680.
[23] V.S. Raghuwanshi, B. Yu, C. Browne, G. Garnier, Reversible pH responsive bovine serum albumin hydrogel sponge nanolayer, Front. Bioeng. Biotechnol. 8 (2020) 573.
[24] O. Glatter, O. Kratky, Small Angle X-ray Scattering, Academic Press, London, New York, 1982.
[25] V.S. Raghuwanshi, U.M. Garusinghe, W. Batchelor, G. Garnier, Polyamide-amine-epichlorohydrin (PAE) induced TiO2 nanoparticles assembly in cellulose network, J. Colloid Interface Sci. 575 (2020) 317–325.
[26] V.S. Raghuwanshi, A. Gallos, D.J. Mendoza, M. Lin, F. Allais, G. Garnier, Nanocrystallisation and self-assembly of biosourced ferulic acid derivative in polylactic acid elastomeric blends, J. Colloid Interface Sci. 606 (2022) 1842–1851.
[27] T.G. Parton, R.M. Parker, G.T. van de Kerkhof, A. Narkevicius, J.S. Haataja, B. Frka-Petesic, S. Vignolini, Chiral self-assembly of cellulose nanocrystals is driven by crystallite bundles, Nat. Commun. 13 (1) (2022) 2657.
[28] D. Qu, M. Archimi, A. Camposeo, D. Pisignano, E. Zussman, Circularly polarized laser with chiral nematic cellulose nanocrystal cavity, ACS Nano 15 (5) (2021) 8753–8760.
[29] C.J. Mable, R.R. Gibson, S. Prevost, B.E. McKenzie, O.O. Mykhaylyk, S.P. Armes, Loading of silica nanoparticles in block copolymer vesicles during polymerization-induced self-assembly: encapsulation efficiency and thermally triggered release, J. Am. Chem. Soc. 137 (51) (2015) 16098–16108.
[30] M.A. Boles, M. Engel, D.V. Talapin, Self-assembly of colloidal nanocrystals: from intricate structures to functional materials, Chem. Rev. 116 (18) (2016) 11220–11289.
[31] K. Kubiak-Ossowska, K. Tokarczyk, B. Jachimska, P.A. Mulheran, Bovine serum albumin adsorption at a silica surface explored by simulation and experiment, J. Phys. Chem. B 121 (16) (2017) 3975–3986.
[32] H. Thérien-Aubin, A. Lukach, N. Pitch, E. Kumacheva, Coassembly of nanorods and nanospheres in suspensions and in stratified films, Angew. Chem. Int. Ed. 54 (19) (2015) 5618–5622.
[33] ⟨http://archive.synchrotron.org.au/aussyncbeamlines/saxswaxs/software-saxs waxs⟩.
[34] P.A. Kralchevsky, K. Nagayama, Capillary forces between colloidal particles, Langmuir 10 (1994) 23–36.
[35] D.Y.C. Chan, J.D. Henry, L.R. White, The interaction of colloidal particles collected at fluid interfaces, J. Colloid Interface Sci. 79 (1981) 410–418.
[36] P.A. Kralchevsky, V.N. Paunov, N.D. Denkov, I.B. Ivanov, K. Nagayama, Energetical and force approaches to the capillary interaction between particles attached to a liquid -fluid interface, J. Colloid Interface Sci. 155 (1993) 420–437.
[37] P.J. Rivero, J. Goicoechea, I. Raul Matias, F.J. Arregui, A comparative study of two different approaches for the incorporation of silver nanoparticles into layer-by-layer films, Nanoscale Res. Lett. 9 (2014) 301.
[38] X. Chen, J. Schröder, S. Hauschild, S. Rosenfeldt, M. Dulle, S. Förster, Simultaneous SAXS/WAXS/UV−Vis study of the nucleation and growth of nanoparticles: a test of classical nucleation theory, Langmuir 31 (42) (2015) 11678–11691.